Flexible and Ultra-thin Metal-Oxide films for multi resonance-based Sensors in Plastic Optical Fibers

N. Cennamo, F. Arcadio, L. Noel, L. Zeni, O. Soppera

To cite this version:

N. Cennamo, F. Arcadio, L. Noel, L. Zeni, O. Soppera. Flexible and Ultra-thin Metal-Oxide films for multi resonance-based Sensors in Plastic Optical Fibers. ACS Applied Nano Materials, 2021, 4 (10), pp.10902-10910. 10.1021/acsanm.1c02345 . hal-03367555

HAL Id: hal-03367555
https://hal.science/hal-03367555v1

Submitted on 6 Oct 2021

Flexible and Ultra-thin Metal-Oxide films for multi resonance-based Sensors in Plastic Optical Fibers

N. Cennamo[1], F. Arcadio[1], L. Noel[2,3], L. Zeni[1], and O. Soppera[2,3,*]

[1]Department of Engineering, University of Campania Luigi Vanvitelli, 81031 Aversa, Italy

[2]Université de Haute Alsace, CNRS, IS2M UMR 7361, 68100, Mulhouse, France

[3]Université de Strasbourg, Strasbourg, France

*e-mail: olivier.soppera@uha.fr

***Abstract*- We have exploited a laser-based integration process of ultra-thin Metal-Oxide (MO) films in order to improve the plasmonic effect in sensors based on D-shaped Plastic Optical Fibers (POFs). More specifically, by using ultra-thin MO films, the performances of the Surface Plasmon Resonance (SPR) phenomenon improve and a Lossy Mode Resonance (LMR) can occur. Although the role of this kind of materials has been already presented, when they are deposited as overlayer (upside the thin metal film), we have used a different approach by depositing MOs, specially Zirconium Oxide (ZrO_2) and Titanium Oxide (TiO_2), as flexible intermediate layers between the exposed core of POFs and the gold film. The MO layer is prepared from sol-gel solution and Deep-UV laser curing allows to densify the thin film and tune the refractive index, with a room temperature process fully compatible with the flexible polymer substrates. In a preliminary step, we have carried out numerical results, based on transfer matrix formalism, in order to predict the SPR response. Subsequently, we have experimentally characterized the developed sensor configurations. Numerical and experimental results have shown above all an enhancement of the sensor performances, in terms of SPR sensitivity, with respect to a reference sensor based on a polymer instead of MOs. Moreover, in some proposed sensor configurations, together with the SPR phenomenon, an LMR phenomenon was observed. It occured in a different wavelength range, for a typical refractive index range present when considering receptors for biochemical sensing applications. Therefore, both resonances (SPR and LMR) could be used in several application fields.**

Keywords: plasmonic sensors, optical fibers, metal oxide layers, deep-ultraviolet curing, sol-gel

I. INTRODUCTION

Surface Plasmon Resonance (SPR) and Localized SPR (LSPR) are well-known techniques, widely used both in academic and commercial areas, because of their great sensitivity and versatility in several application fields [1-5]. In particular, the plasmonic phenomenon is very sensitive to the change in the refractive index of a dielectric medium in contact with a noble metal thin film (e.g. gold). Moreover, Lossy Mode Resonance (LMR) complements the metallic materials typically used in SPR–based sensors, with thin metallic oxides and polymers [6,7].

To realize even more efficient sensor systems, SPR, LSPR, and LMR can be coupled with optical fibers so taking advantage of the excellent properties related to these guiding structures, like immunity to electromagnetic interferences, the possibility of remote sensing and so on [6-13]. Along this line, several configurations have been exploited in literature, like the ones based on D-shaped fibers [14-17], tapered fibers [18-21], U-bent fibers [22,23], and many others [24-26]. In the last years, in order to improve the performances of SPR sensors based on optical fiber, several measures have been adopted, like, for instance, by using ultra-thin films graphene-based, that have led to excellent results [27-29].

With the aim to obtain an improved SPR platform, Cennamo et al. have presented a plasmonic platform based on a D-shaped plastic optical fiber (POF) that includes an intermediate buffer layer between the fiber core and the gold film [15]. This layer, having a refractive index higher than the one of the fiber core, is above all useful to improve the adherence of the subsequent layers and, moreover, its use leads to an enhancement of the performances in terms of signal to noise ratio (SNR) [15]. The aim, in order to emphasize this aspect, is to reduce the thickness of the intermediate layer and in the same time to increase its refractive index. To do this, a possible alternative is represented by Metal-Oxide (MO) layers, that have already demonstrated to be an appropriate solution to achieve what wished when are deposited as overlayer [30-33]. In particular, metal oxides are relevant because they are suitable in different application fields, ranging from optics to photonics and microelectronics [34-36]. MO are indeed transparent in the visible range, chemically inert, with good mechanical properties and with high refractive index. Among the different processes to integrate MO, processes based on the use of MO precursors in solution (sol-gel chemistry) have been very successful in recent years because they are low-cost techniques, simple to implement and offering multiple possibilities in terms of chemical compositions and associated properties. However, one of the important limitations to the integration of these materials on flexible substrates (polymer films, polymer fibers for example) is the need for a thermal treatment step at relatively high temperature to remove the solvent, the organic part of the precursors and to densify the material. Typically, temperatures in the range of 300°C to 600°C are required, depending on the precursors and the desired material [37]. Soppera et al proposed a process based on Deep-UV (193 nm) excimer laser irradiation for curing the deposited wet film and obtaining the MO thin film. The interest of this approach is to reduce the curing time, introduce the possibility to locally treat the material for photopatterning, and above all, be suitable with polymer substrates since the process is led at room temperature. [38-41].

In this work we propose several multi-resonance POF sensor configurations, based on a D-shaped POF platform, implementing different ultra-thin MOs films, specially Zirconium Oxide (ZrO_2) and Titanium Oxide (TiO_2), as intermediate layers between the exposed core of the POF and the gold film. This choice is contingent on the fact that we want to keep gold as external layer in order to harness the optimized functionalization processes, when considering bio-chemical sensing applications. Several ultra-thin MOs films combined with metal nanofilms have been theoretically studied, by performing numerical simulation with a commercially available software, for plasmonic sensor configurations different from the ones proposed in this work [42-44]. At first, we present the conditions to prepare the thin films and their characterization by spectroscopic ellipsometry and FTIR. Then, we have conducted a numerical analysis, based on transfer matrix formalism, to predict the SPR behavior of these novel configurations; subsequently, we have realized and tested these MO-based POF sensors and then compared the performances, in terms of sensitivity, with respect to a reference sensor (it is based on the same D-shaped POF with a photoresist buffer layer, used as intermediate layer [15]). Moreover, we have highlighted that some sensor configurations show, in addition to the SPR phenomenon excited independently from the polymer buffer layer [15] in the range from 600 nm to 770 nm, also a tangible LMR phenomenon in the range from 500 nm to 540 nm, so making it possible to monitor both resonances (SPR and LMR), when these platforms are used in biochemical sensing applications.

II. MATERIALS AND METHODS

A. SPR-POF reference sensor

The construction process of the SPR-POF reference sensor, schematically reported in **Figure S1a**, is extensively described in [15] and includes a plastic optical fiber having a poly(methyl methacrylate) (PMMA) core of 980 μm diameter (refractive index equal to 1.49) and a fluorinated cladding (refractive index equal to 1.41) of 10 μm diameter (1 mm total diameter). The POF is embedded in a resin block implementing a specific trench and is then lapped, to remove the cladding and part of the core, with two different polishing papers (1 μm and 5 μm grits). The next step consists in depositing, through a spin coater, a 1 μm thick Microposit® S1813 photoresist buffer layer (refractive index equal to 1.61) on the exposed core of the POF. Finally, a 60 nm thick gold layer is deposited through a sputtering machine (BalTec SCD 500). The sputtering process is split in three equal steps with a current of 60 mA and a deposition time of 35 s (20 nm per step) to guarantee a low temperature process. A schematic cross section of the SPR-POF reference sensor is shown in **Figure S1b** with the refractive indices and the dimensions.

B. *Chemicals to realize MO films*

Titanium (IV) tetraisopropoxide (97%) and zirconium (IV) tetrapropoxide (70% in n-propanol) were purchased from Merck, and used as received. Methacrylic acid (99%) was also purchased from Merck, and n-propanol (99%) from Alfa Aesar.

Titanium and Zirconium precursors solutions were prepared following the same protocol described in [41]. Firstly, the metal alkoxide precursor was mixed with methacrylic acid (MAA) and stirred for 5 minutes. Then, 2 ml n-propanol was added, and the solution was stirred for ten more minutes, before the addition of de-ionized water (DI). The formulations were prepared in order to respect molar ratios of Ti:MAA:DI=1:8:20 and Zr:MAA:DI=1:10:22, in order to prepare Ti- (TiOC) and Zr-oxo clusters (ZrOC) solutions, respectively. The resulting formulation was stirred for an extra hour and an ageing step of 24 hours was required. In order to obtain a specific viscosity, the dilution rate was adjusted after these 24 hours by adding a precise amount of n-propanol, varying from 4 to 24 ml.

C. *Deposition, Deep-UV laser curing and characterization of ultra-thin MO films*

The metal oxide films were deposited by spin-coating at 3000 rpm for 60s. The optical characterizations were performed by spectroscopic ellipsometry (UVISEL ellipsometer from Horiba-Jobin-Yvon). P-type silicon wafers (purchased from Siegert) were used for the optical characterization by ellipsometry. These substrates were cleaned by ethanol and acetone, and were placed in a UV-ozone cleaner.

The FTIR measurements were performed on a Thermo Scientific Nicolet iS50 spectrometer, in ATR (attenuated total reflection) mode, using a Ge Angle grazing prism, variGATR (64° for our measurements).

Deep-UV laser curing was done by using an ArF excimer laser (193nm, Braggstar from Coherent). Power was typically set to 2 mW/cm^2 (20 Hz).

Two kind of thin films were prepared, named monolayer and bilayer designs. For monolayer designs, the thin films were obtained by a unique deposition step (spin-coating, 3000rpm for 60s) and cured by a single DUV-exposure (2000 mJ·cm^{-2}). The viscosity of the solution was adapted to obtain the target thickness (80 nm). The bilayer design was obtained by two successive deposition and curing steps: the viscosity of the solution (Zr and Ti precursors) was set to obtain 40 nm thickness thin films and the exposure energy was 1000 mJ·cm^{-2} for each layer. In the bilayer design, both materials can be combined.

Each design was characterized by performing an ellipsometry measurement from 1.5 to 5 eV. DeltaPsi2 (DP2) software was used to determine both the refractive index and the thickness of each layer separately and in the stack. For the TiO_2 and ZrO_2 layers, a Tauc-Lorentz dispersion formula and a classical oscillator model were respectively selected to correctly fit the experimental data. The classical oscillator model includes a high frequency constant and a Lorentz oscillator.

To improve the performances of the SPR-POF sensors we have replaced the photoresist layer present in the reference sensor [15] with different ultra-thin films of metal oxides, deposited and optically characterized in the previous section III.

Figure 1 shows the schematic preparation of SPR-POF-MO configurations and the cross section of each.

In particular, we have exploited four different sensor configurations, by keeping fixed a total thickness of 80 ± 2 nm for the intermediate layer: a ZrO_2 single layer ("Monolayer design 1" in **Fig. 1b**); a TiO_2 single layer ("Monolayer design 2" in **Fig. 1c**); a bilayer ZrO_2-TiO_2 ("Bilayer design 1" in **Fig. 1d**) including a ZrO_2 layer (thickness of about 40 ± 2 nm) in contact with the core of the fiber and a TiO_2 layer (thickness of about 40 ± 2 nm) on the top; a bilayer TiO_2-ZrO_2 ("Bilayer design 2" in **Fig. 1e**), similar to the latter but obtained by swapping the position of the metal oxides.

In a final step, we have sputtered a 60 nm thick gold layer over all the configurations, such as in the case of the reference sensor [15].

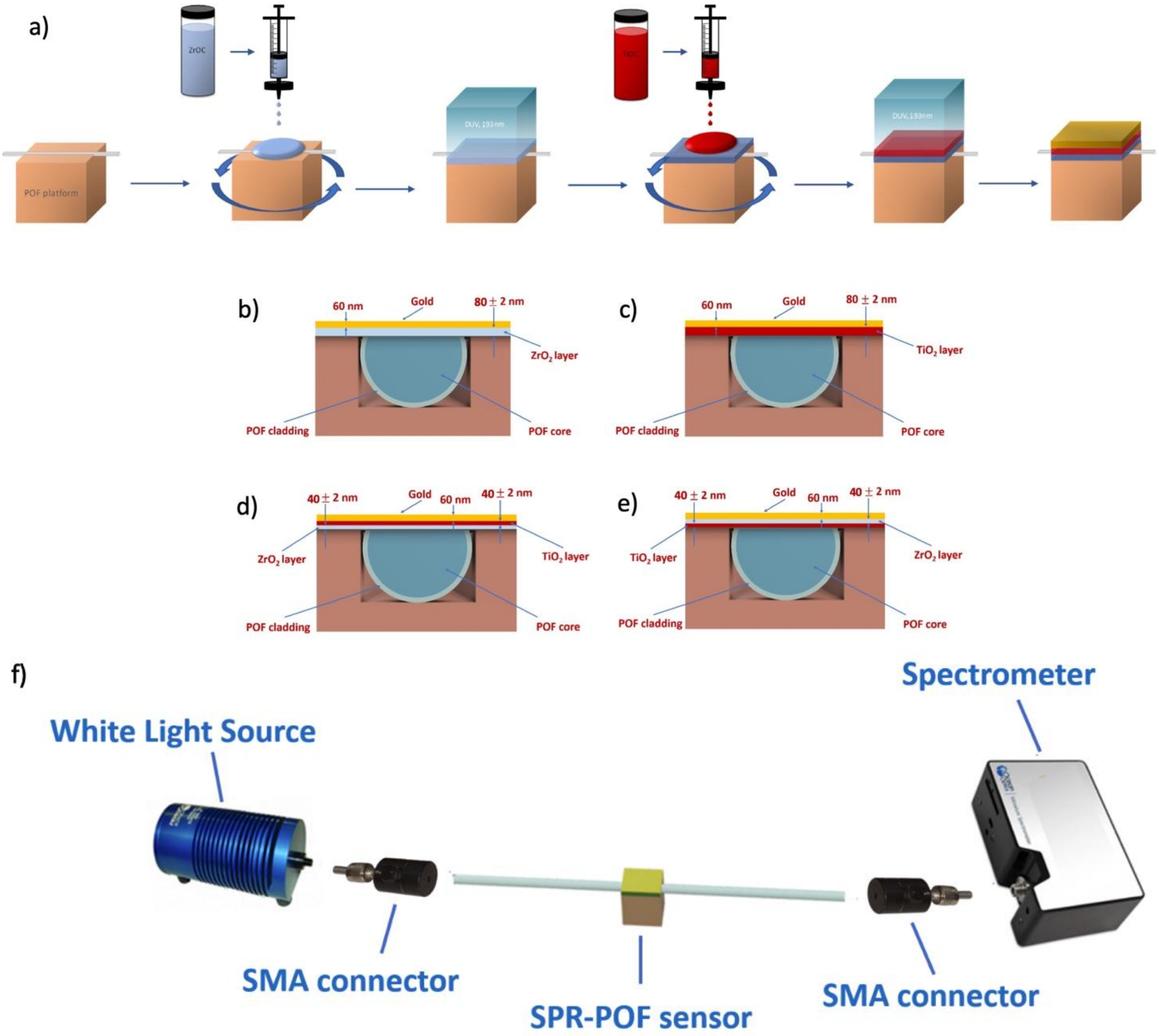

Figure 1. (a) Schematic of the SPR-POF-MO preparation and schematic cross sections of the SPR-POF-MO configurations: (b) Monolayer design 1; (c) Monolayer design 2; (d) Bilayer design 1 and (e) Bilayer design 2; (f) Outline of the experimental setup.

D. Experimental setup

To experimentally test the aforementioned configurations, we have used a simple and low-cost experimental setup. It includes: the halogen lamp, used as white light source (HL-2000-LL, manufactured by Ocean Optics, Dunedin, FL, USA), that emits in a spectral range between 360 nm and 1700 nm; the POF sensor; the spectrophotometer (FLAME-S-VIS-NIR-ES, manufactured by Ocean Optics, Dunedin, FL, USA), able to detect in a spectral range between 350 nm and 1023 nm with a spectral resolution equal to 1.5 nm full width at half maximum (FWHM). More in detail, two SMA connectors have been used to connect the plasmonic sensors both to the white light source and the spectrometer. **Fig. 1f** shows an outline of the described setup, used to carry out all the experimental measurements.

Moreover, we have tested both the SPR-POF reference sensor and the SPR-POF-MO configurations by using different water-glycerin solutions, that have a refractive index ranging from 1.332 to 1.411. These values have been determined, in a first place, by an Abbe refractometer (Model RMI, Exacta + Optech GmbH, Munich, Germany). These solutions are applied to obtain the bulk sensitivity of the tested plasmonic sensors.

III. High refractive index thin film layer preparation and characterization

As explained in the introduction, we developed a specific photoresist that is based on transition metal complexes, with an integration process that is compatible with the POF platform. Indeed, this photoresist can be displayed by spin-coating and cured by DUV laser, at room temperature to form a high refractive index thin film that improves the optical response of the sensor. Since this photoresist is home-made, we provide in this section information on the preparation and characterization, showing some specific features and interest in this context.

Figure S2 shows the typical range of thickness and refractive index achievable using the Ti and Zr-based photoresist, with various dilution factors and DUV laser curing energy. A significant modification of these two parameters was recorded with DUV irradiation, which allows to tune the properties of the thin film in a wide range with simple parameters.

In order to describe the structure of the material after DUV irradiation, FTIR spectra (ATR mode) were recorded for the deposited films and after irradiations of 1000 mJ/cm^2 and 2000 mJ/cm^2. These spectra are given in **Figure S3**, for Ti and Zr based resins (resp. **S3.a** and **S3.b**).

In both cases, characteristic bands of organic ligands (complexed methacrylic acid) are found at 1550 et 1420 cm^{-1}. These results are in agreement with previously published results. [45, 46] These bands disappear almost completely in the case of Ti-based resins, which shows that the material after 1000 mJ/cm^2 is still a hybrid material with organic functions but that after 2000 mJ/cm^2, it is mainly inorganic (TiO_2). In the case of ZrO_2, the hybrid to inorganic conversion is not complete, even after 2000 mJ/cm^2, as shown by an important contribution of the bands around 1400 cm^{-1}. However, we will adopt the notation ZrO_2, for simplification in the following, even if the material is not completely inorganic in this case. Note that the decrease of the organic part in the material is accompanied by a significant increase of broad bands centered at 3400 cm^{-1} which can be attributed to hydroxyls (TiOH and ZrOH), resulting from the removal of organic ligands. These results are in agreement and complete the analyses presented in previous works by Stehlin at al.[41]

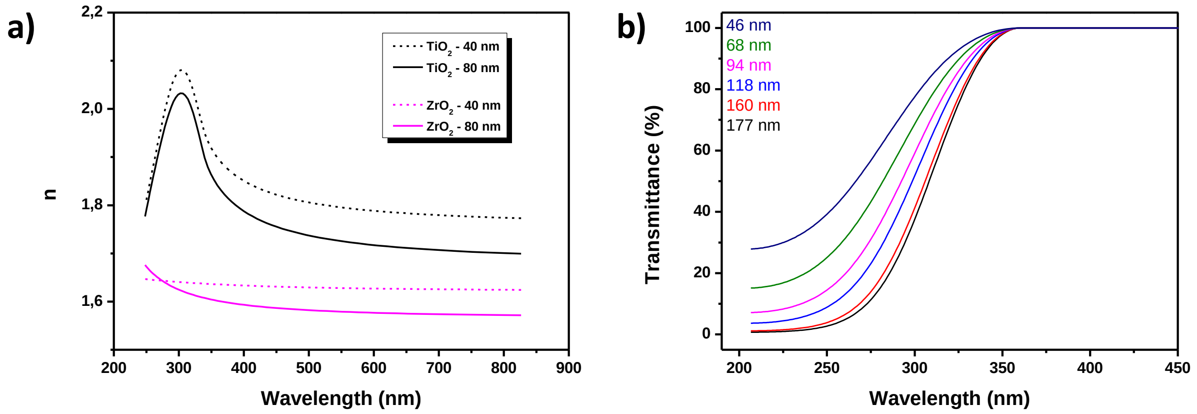

Figure 2. a) Dispersion curves of TiO_2 and ZrO_2 thin films obtained by spectroscopic ellipsometry for 40 and 80 nm thickness. b) are the transmittance curves of the TiO_2 thin films with various thicknesses.

Films with thicknesses of 40 and 80 nm were chosen in the following (with respective energy of 1000 mJ/cm^2 and 2000 mJ/cm^2). The dispersion curves of such thin films are given in **Figure 2.a**. We note that slight discrepancies are present between the 40 nm and 80 nm layers due to the effect of the DUV light absorption within the film. Indeed, as shown in **Figure 2.b**, the metal complexes thin films present a strong absorption at the irradiation wavelength (193 nm). This feature is important to provide a good photosensitivity of the photoresist but also explains this effect due to internal filter effect.

Table 1: Geometrical and optical parameters of the SPR-POF-MO configurations

Configuration	Metal-oxides	Thickness [nm]	n at 633 nm
Monolayer design 1	ZrO_2	80 ± 2	1.59
Monolayer design 2	TiO_2	80 ± 2	1.71
Bilayer design 1	ZrO_2-TiO_2	40 ± 2 (ZrO_2) + 40 ± 2 (TiO_2)	1.63 (ZrO_2) and 1.79 (TiO_2)
Bilayer design 2	TiO_2-ZrO_2	40 ± 2 (TiO_2) + 40 ± 2 (ZrO_2)	1.79 (TiO_2) and 1.63 (ZrO_2)

Table 1 summarizes the thicknesses and the refractive indices for each considered layer. It is important to underline that the goal of this work is not to optimize the thicknesses of these layers but to replace the photoresist layer present in the reference sensor [15] with these ultra-thin films of metal oxides to emphasize their key aspects in the plasmonic phenomena, related to their material nanometric dimensions and their very high refractive indices.

IV. SPR NUMERICAL ANALYSIS

In order to perform an SPR numerical analysis, we have considered an N-layer approximation model by taking advantage of the transfer matrix formalism [47]. It should be stressed that the used numerical approach does not contemplate the LMR phenomenon. In such a way, we have simulated the SPR response and then compared the performances in terms of bulk sensitivity for both the reference sensor and all the MO-based configurations. In particular, **Figure 3a** shows the resonance wavelength shift ($\Delta\lambda$), calculated with respect to the water (n=1.332), versus the refractive index, along with the quadratic fitting to the numerical data. The simulated SPR spectra at varying of the external refractive index, for all the sensor configurations, have been reported in **Figure S4** (Supporting Information).

The simulation results shown in **Fig. S4**, have been calculated by taking the ratio between the transmitted spectrum for a given refractive index of the external medium (from 1.332 to 1.411), and the transmission spectrum in air. It can be noticed that the normalized transmitted spectra at wavelengths minor then 650 nm is higher than unity because, at those wavelengths, the transmission with liquid as cladding is higher than transmission with air as cladding. In turns, this depends on the fact that, for most of the angles of incidence of the transmitted light, the reflection coefficient at the fiber interface is higher when the metal film is in contact with the liquid, than when the metal is in contact with air.

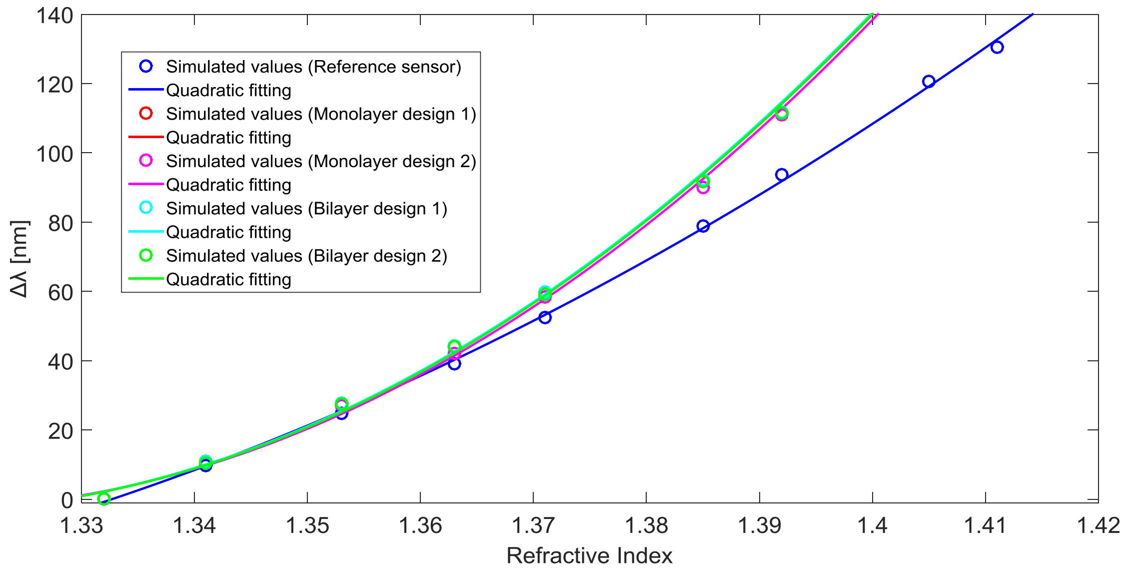

(a)

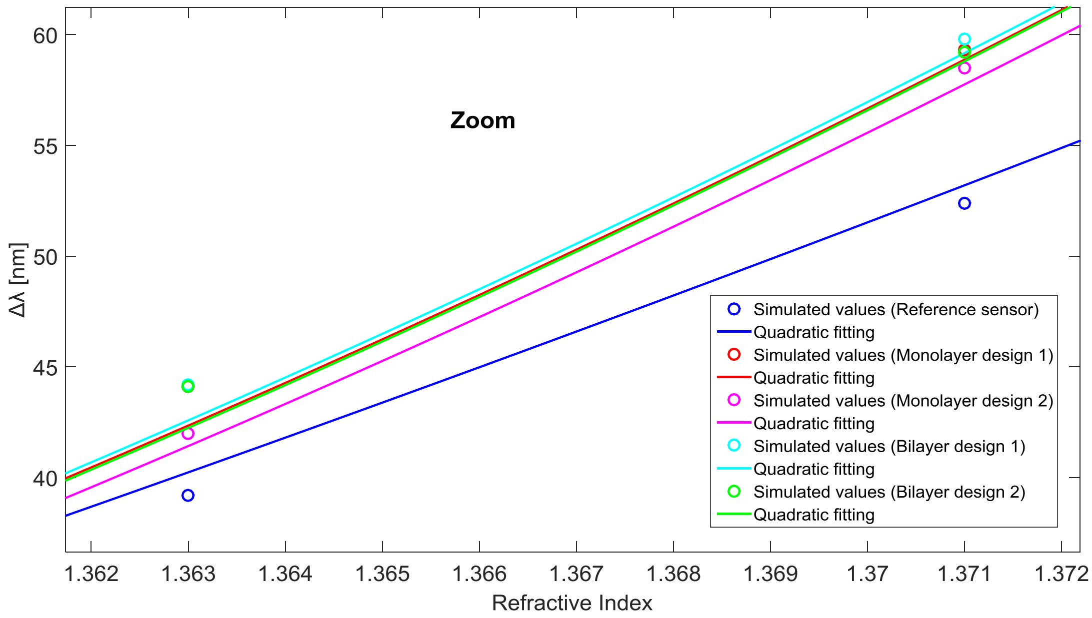

(b)

Figure 3. (a) Resonance wavelength shift (Δλ) versus refractive index, calculated with respect water (n=1.332), along with quadratic fitting of the simulated values. (b) Zoom relative to the refractive index range from 1.362 to 1.372.

Equation 1 represents the fitting curve reported in **Figure 3a**, while in Table 2 are listed the relative parameters for all the simulated sensor configurations.

$$\Delta\lambda = \mathrm{A}\, n^2 + B\, n\, + \mathrm{C} \tag{1}$$

where $\Delta\lambda$ is the variation in resonance wavelength with respect water (n=1.332), *n* represents the refractive index of the solution in contact with the plasmonic sensor, whereas *A*, *B*, and *C* represent the parameters relative to the quadratic fitting curves used to interpolate the simulated data.

For some MO sensor configurations, the numerical responses are very similar (we can see that we have overlapping lines in **Figure 3a)**. This aspect can also be examined by the fitting parameters reported in Table 2. This characteristic is due to the used approximated numerical model. To show the minor differences, **Figure 3b** shows a zoom of **Figure 3a** in the refractive index range from 1.362 to 1.372.

Table 2: Fitting parameters relative to Equation (1) for the simulated SPR-POF and SPR-POF-MO sensor configurations

Configuration	A	B	C	Adj. R-square
Reference sensor	7638.3	-19263	12106	0.999
Monolayer design 1	19758	-51955	34150	0.998
Monolayer design 2	19981	-52586	34597	0.999
Bilayer design 1	19792	-52038	34202	0.998
Bilayer design 2	19881	-52286	34374	0.998

For these kinds of sensors, the performances can be analyzed by considering the bulk sensitivity (S) [15] that can be defined as [15,47]:

$$S(n) = \frac{\delta\lambda}{\delta \mathrm{n}} \left[\frac{nm}{RIU}\right] \tag{2}$$

where δn represents the alteration in the refractive index of the solution upon the SPR platform, which produces a variation in resonance wavelength equal to δλ. In equation 2, we have reported the partial derivative to indicate that the resonance wavelength is a function of several parameters (e.g. the refractive indices of the waveguide, the thickness of the gold film, etc.).

Considered Equation 2, using the fitting curves described in Equation 1, with the relative parameters reported in Table 2, we can approximate the bulk sensitivities as the first derivative of the quadratic functions, as reported in Equation (3), for all the simulated configurations.

$$S(n) = 2\mathrm{A}\,n + B \quad \left[\frac{nm}{RIU}\right] \qquad (3)$$

These approximated bulk sensitivities are reported in **Figure 4**, where a significant improvement in sensitivity, in the refractive index range from 1.35 to 1.42, can be observed when MOs are used instead of a photoresist buffer layer, even if the differences between the MO-based sensor configurations can not be examined.

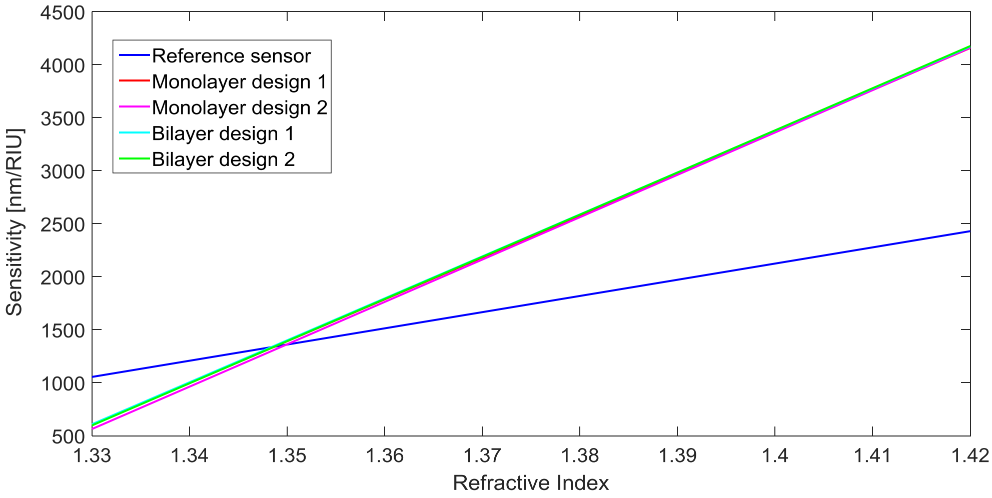

Figure 4. SPR Sensitivity as a function of the refractive index for all the simulated configurations.

V. RESULTS AND DISCUSSION

A. SPR analysis

In a first step, we have tested both the SPR-POF reference sensor and the SPR-POF-MO sensor configurations in order to carry out a comparative analysis. In the refractive indices range tested, the SPR phenomenon is present in the wavelength range from 600 nm to 770 nm, similar to [15] where the configurations with and without the polymer buffer layer are compared. Thus, for each configuration, in **Figure 5** are reported the experimentally obtained SPR spectra (for all the tested configurations) and the variation in SPR resonance wavelength ($\Delta\lambda_{SPR}$), with respect water (n=1.332), versus the refractive index (*n*), together with the quadratic fitting (Eq. 1) of the experimental data and the error bars. In **Figure 5f** each experimental value is the average of 3 measurements obtained by the same sensor, in three different measurements. The error bars reported in **Figure 5f** are calculated as the max measured standard deviation (it is equal to 0.2 nm).

Comparing **Figure 5f** (experimental results) with **Figure 3a** (simulations), it can be observed that some differences between the SPR-POF-MO configurations are present in the experimental results, whereas they are not appreciated in the simulations.

Table 3 reports the fitting parameters (see Eq. 1) relative to all the tested sensor configurations.

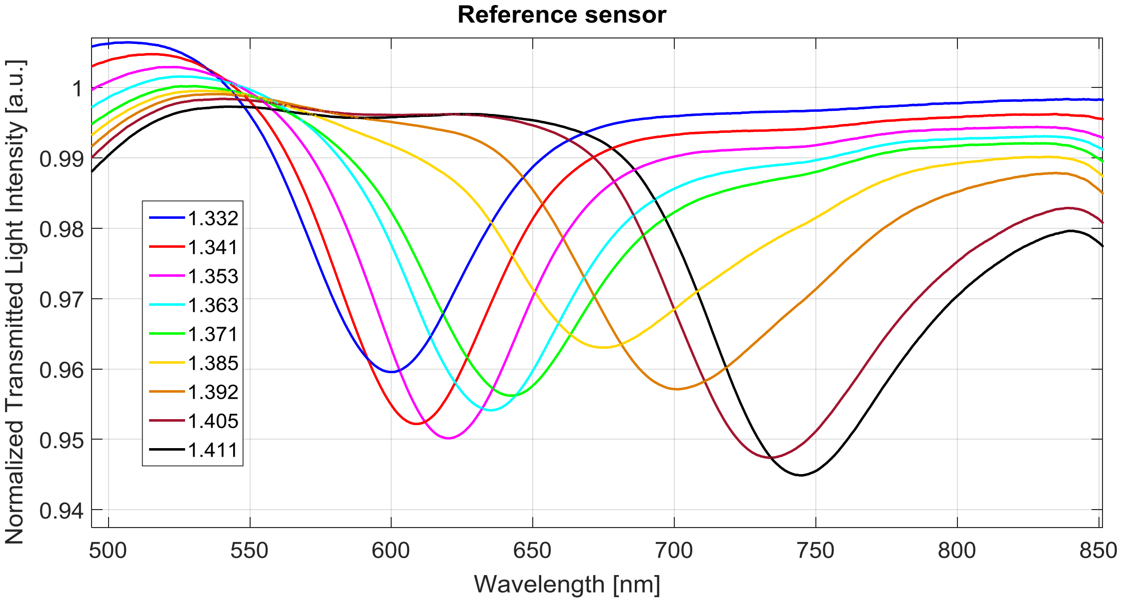

(a)

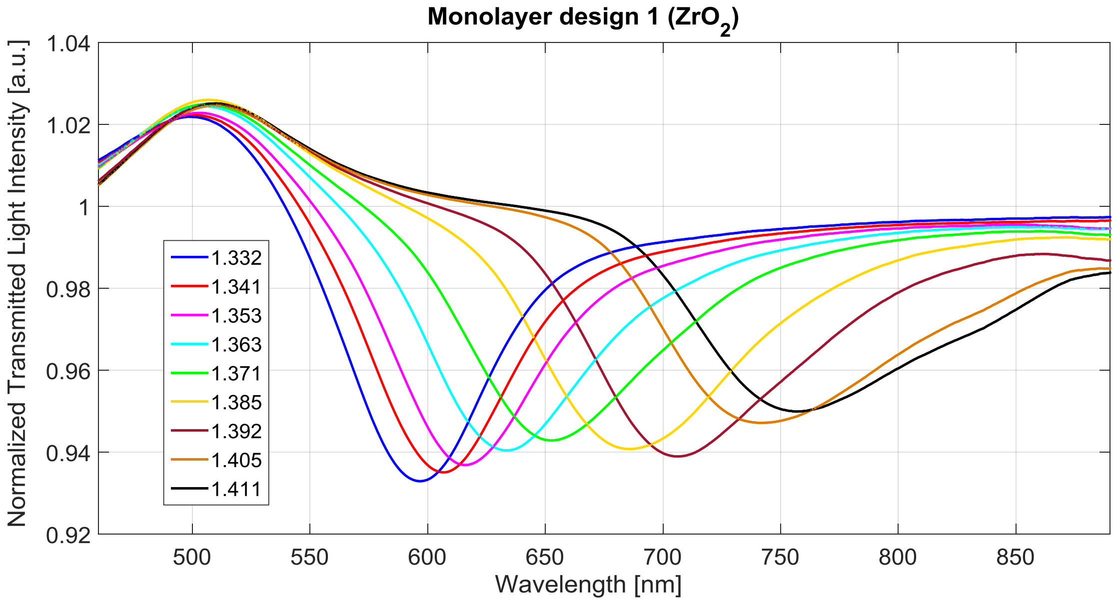
Monolayer design 1 (ZrO_2)
Normalized Transmitted Light Intensity [a.u.]
1.04
1.02
1
0.98
0.96
0.94
0.92
500
550
600
650
700
750
800
850
Wavelength [nm]
1.332
1.341
1.353
1.363
1.371
1.385
1.392
1.405
1.411

(b)

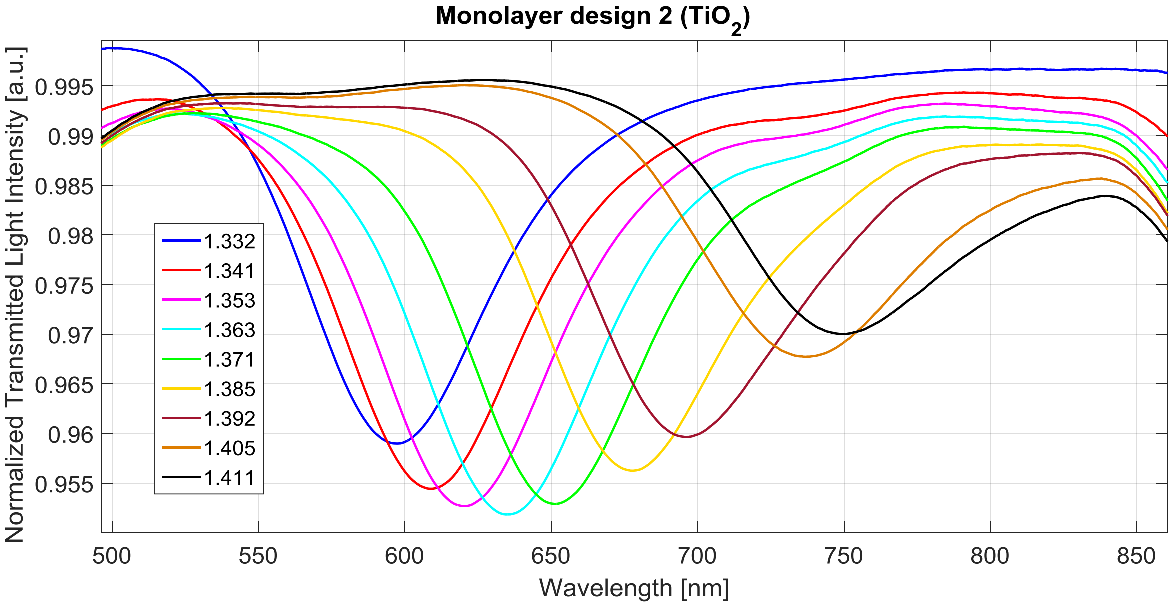
Monolayer design 2 (TiO_2)
Normalized Transmitted Light Intensity [a.u.]
0.995
0.99
0.985
0.98
0.975
0.97
0.965
0.96
0.955
500
550
600
650
700
750
800
850
Wavelength [nm]
1.332
1.341
1.353
1.363
1.371
1.385
1.392
1.405
1.411

(c)

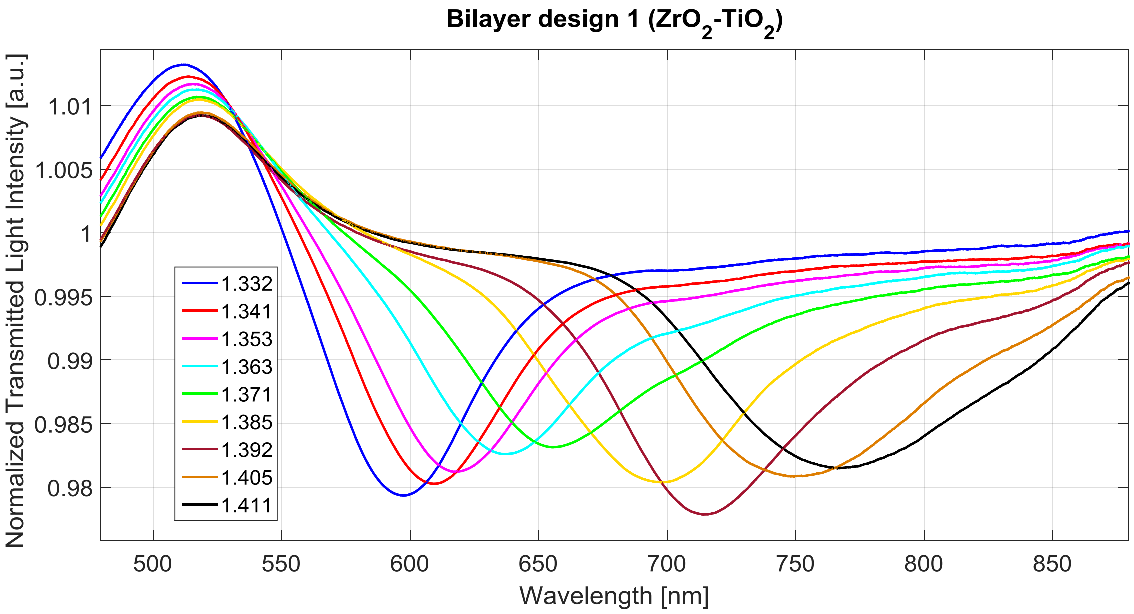
Bilayer design 1 (ZrO_2-TiO_2)
Normalized Transmitted Light Intensity [a.u.]
1.01
1.005
1
0.995
0.99
0.985
0.98
500
550
600
650
700
750
800
850
Wavelength [nm]
1.332
1.341
1.353
1.363
1.371
1.385
1.392
1.405
1.411

(d)

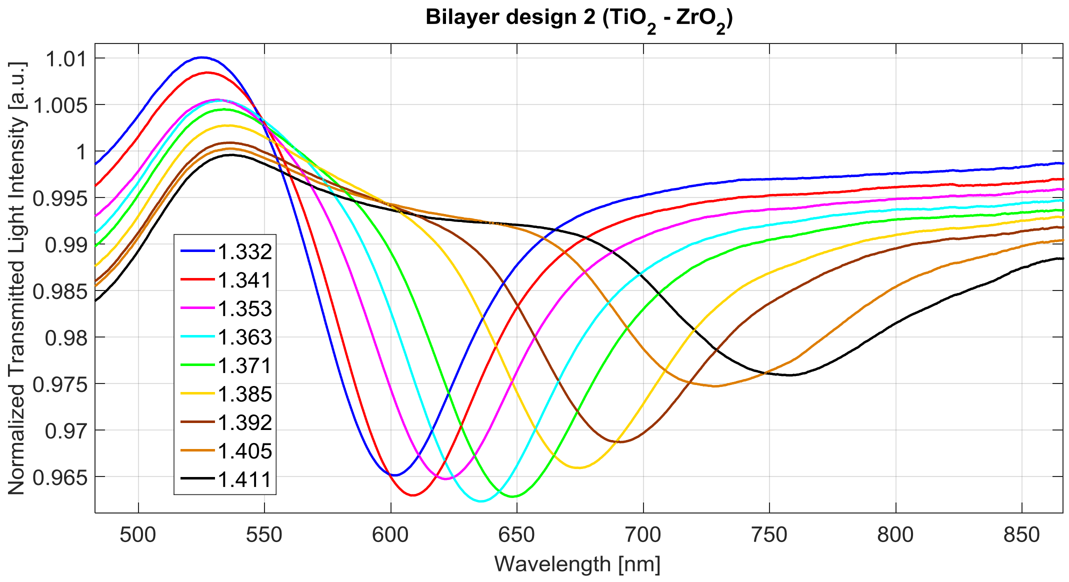
Bilayer design 2 (TiO_2 - ZrO_2)
Normalized Transmitted Light Intensity [a.u.]
1.01
1.005
1
0.995
0.99
0.985
0.98
0.975
0.97
0.965
500
550
600
650
700
750
800
850
Wavelength [nm]
1.332
1.341
1.353
1.363
1.371
1.385
1.392
1.405
1.411

(e)

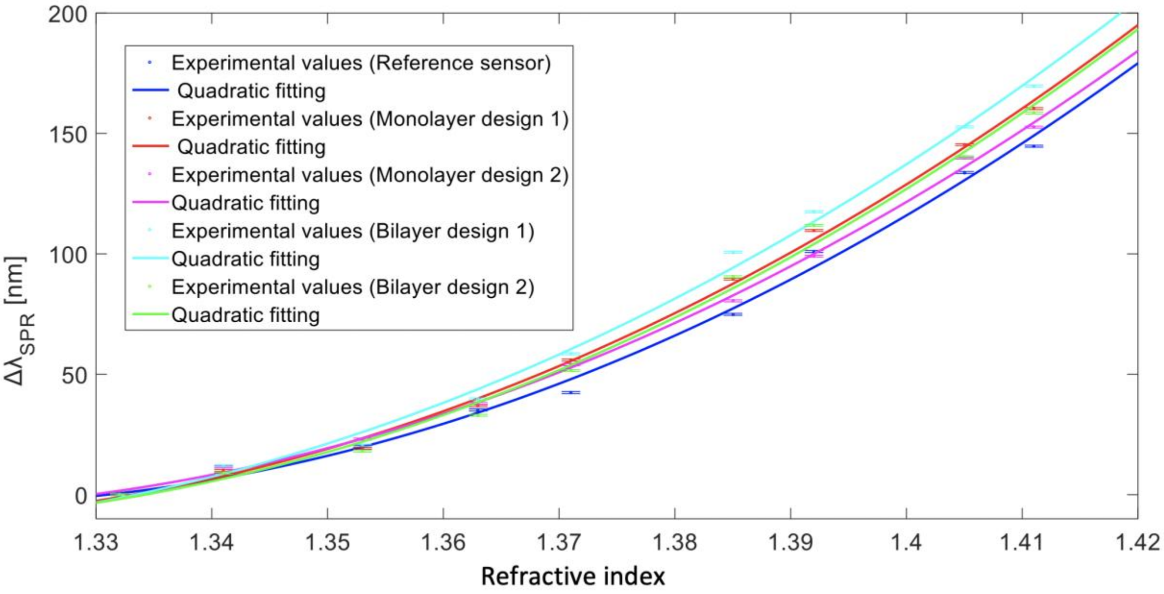

(f)

Figure 5. Normalized SPR spectra experimentally obtained for (a) reference sensor, (b) Monolayer design 1, (c) Monolayer design 2, (d) Bilayer design 1, and (e) Bilayer design 2. (f) Variation of the SPR wavelength ($\Delta\lambda_{SPR}$), calculated with respect to water (n=1.332), versus the refractive index, along with quadratic fitting of the experimental values and error bars.

Table 3: Fitting parameters relative to Equation (1) for experimentally tested SPR-POF and SPR-POF-MO sensors

Configuration	**A**	**B**	**C**	**Adj. R-square**
Reference sensor	16626	-43726	28745	0.993
Monolayer design 1	15906	-41547	27118	0.997
Monolayer design 2	15600	-40857	26745	0.998
Bilayer design 1	15661	-40749	26489	0.994
Bilayer design 2	16160	-42257	27612	0.992

Similarly to SPR numerical results, Equation 1 and Equation 2 make it possible to estimate the bulk sensitivity for all tested sensor configurations, as reported in **Figure 6**. As it is clear, all the SPR-POF-MO configurations present a better SPR bulk sensitivity with respect to the reference sensor, in the considered refractive index range, while the configuration "Bilayer design 1" (ZrO_2-TiO_2) presents the overall better bulk sensitivity.

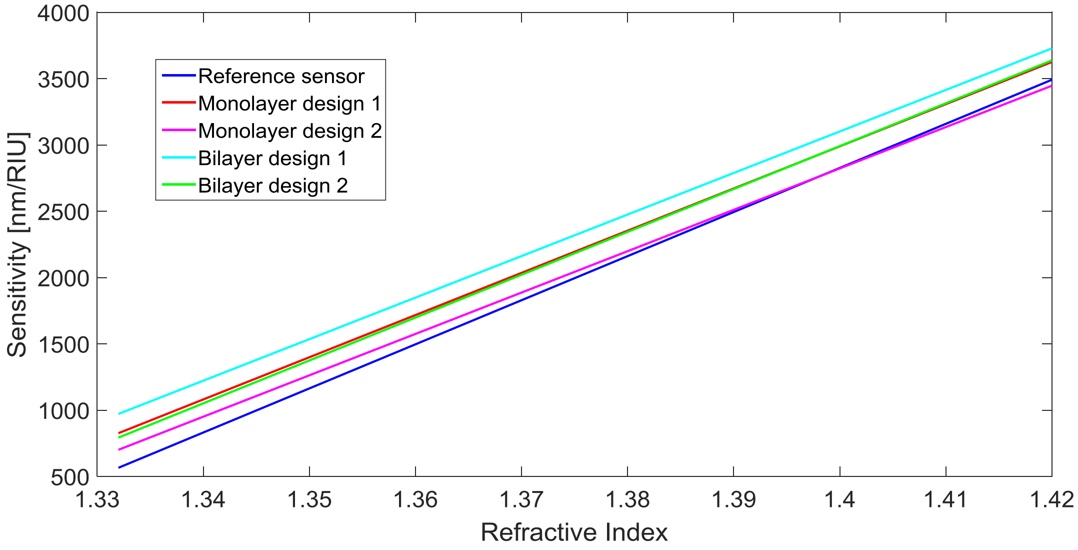

Figure 6. SPR Bulk Sensitivity as a function of the refractive index, for all the tested SPR sensor configurations.

B. LMR analysis

In the considered refractive index range, some sensor configurations have denoted both SPR and LMR phenomena, while in others is more pronounced only the SPR phenomenon. To demonstrate the kind of resonance excited in the wavelength range of about 500 nm, we have experimentally tested the POF sensor configurations based on MOs with and without the gold film. For instance, as reported in **Figure 7** and **Figure 5e,** the configuration "Bilayer design 2" exhibits a similar resonance phenomenon in the wavelength range from 500 nm to 540 nm, with (see **Figure 5e**) and without (see **Figure 7**) the gold nano-film. Similar behaviour has also been observed exploiting the other MO-based sensor configurations without the gold film. Consequently, an LMR phenomenon can be considered in this wavelength range, as also could be examined by the theoretical condition reported in [7]. As well as for the LMR sensors, in both the sensor configurations (with and without the gold film) when the refractive index of the solution increases, the resonance wavelength values increase too (red-shift), as reported in **Figure 5e** and **Figure 7**. Moreover, the SPR phenomenon in the wavelength range from 600 nm to 770 nm (shown in **Figure 5**) is not exited when the gold film is not deposited, as reported in **Figure 7**.

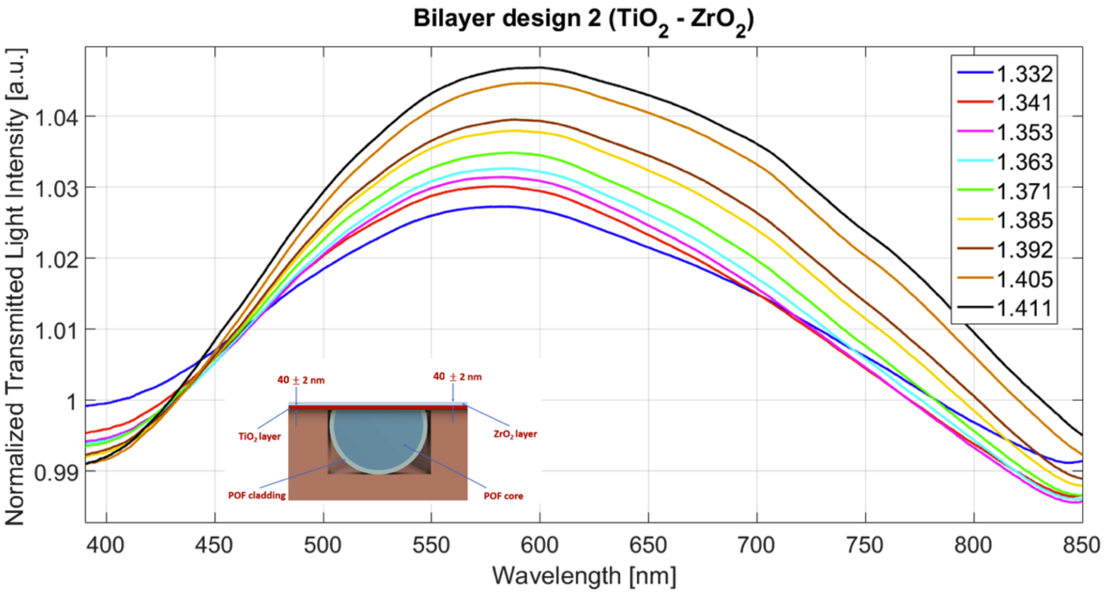

Figure 7. Normalized spectra experimentally obtained for Bilayer design 2 sensor configuration without the gold nano-film.

Figure 8 shows a zoom of the LMR regions for the configurations covered by a gold film in the refractive index range between 1.332 and 1.385, which is typical when considering biosensing applications. As it is clear, for all sensor configurations an increase of the LMR wavelength (around 500 nm) can be noted when the refractive index of the solution increases. Moreover, the normalized intensity value at the LMR resonance wavelength shows a different behavior: in fact, when the refractive index of the solution increases, in the Monolayer design 1 the intensity value increases too whereas in both bilayer configurations it decreases.

This different behaviour (in the intensity value variation) indicates several types of resonance phenomena. In particular, this aspect could be due to the excitation of hybrid modes. So, when monolayer or bilayer are used, different kinds of resonance phenomena are excited.

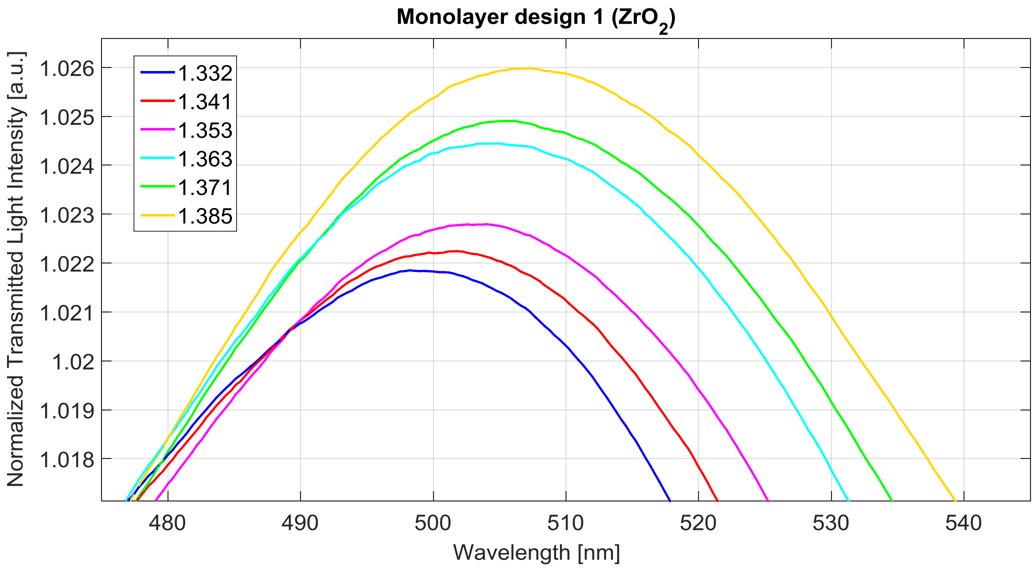

(a)

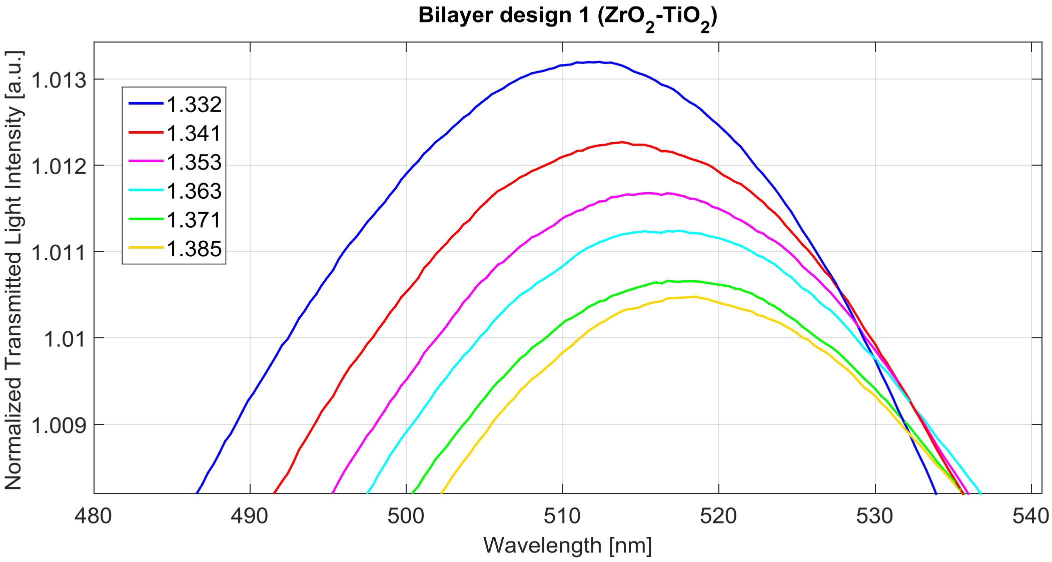

(b)

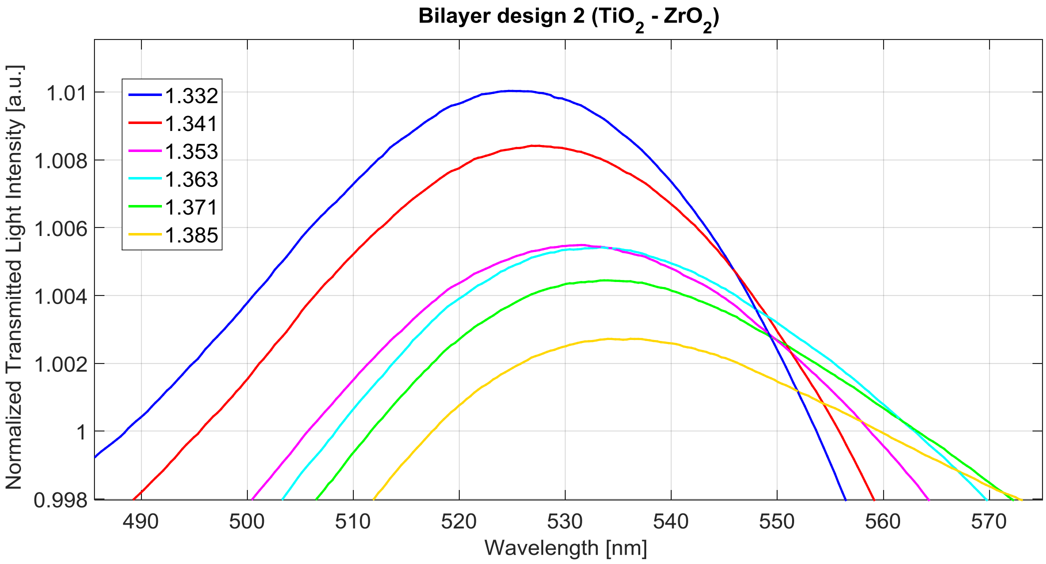

(c)

Figure 8. Normalized LMR transmitted spectra relative to the sensor configurations covered by a gold film: a) “Monolayer design 1”, b) “Bilayer design 1” and c) “Bilayer design 2”.

To carry out a comparative analysis, we have conducted a first order analysis by considering a linear fitting of the experimental values, in the considered refractive index range. In such a way, we have reported in **Figure 9** the variation in LMR wavelength ($\Delta\lambda_{LMR}$) versus the refractive index, for “Monolayer design 1” (**Figure 8a**), “Bilayer design 1” (**Figure 8b**), and “Bilayer design 2” (**Figure 8c**). In **Figure 9** each experimental value is the average of 3 measurements obtained by the same sensor, in three different measurements, whereas the error bars are the max measured standard deviation (0.2 nm).

Standing this, by using **Equation 2**, the bulk sensitivity for these configurations can be approximated with the slopes of the linear fitting functions reported in **Figure 9**, as reported in **Table 4**.

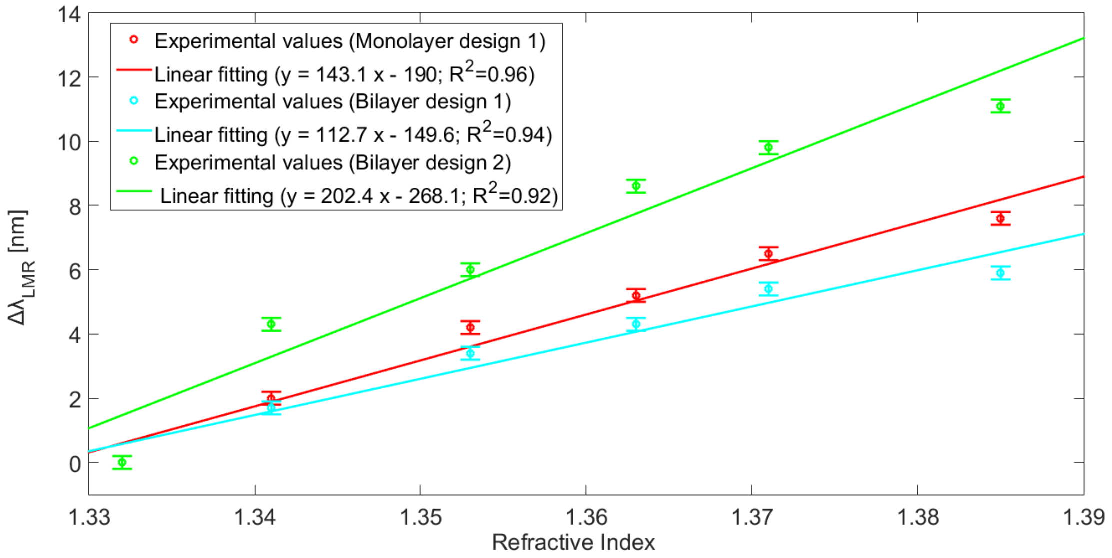

Figure 9. For three different sensor configurations, the variation in LMR wavelength ($\Delta\lambda_{LMR}$) versus refractive index, calculated with respect water (n=1.332) along with linear fitting of the experimental data and error bars.

Table 4: LMR bulk sensitivity for MO-based sensor configurations

Sensor Configuration	**LMR Bulk sensitivity [nm/RIU] (Slope of the linear fitting)**
Monolayer design 1	144.2
Bilayer design 1	100.2
Bilayer design 2	181.1

VI. CONCLUSION

We have implemented several plasmonic sensor configurations, based on a D-shaped POF platform combined with different multilayers (e.g. based on types of metal oxides, specially Titanium Oxide and Zirconium Oxide, and gold film). At first, the numerical results, based on multilayer approximation and transfer matrix formalism, have predicted the goodness of the proposed approach, in term of SPR effect.

The developed sensor configurations have been then experimentally characterized, by using different water-glycerin mixtures whose refractive index ranges from 1.332 to 1.411. The experimental results have shown an overall improvement in the performances in terms of SPR bulk sensitivity, if compared to a reference sensor [15], based on the same D-shaped POF, but with a thicker photoresist layer, as an intermediate layer, instead of MOs.

Moreover, in the considered refractive index range, we have denoted a marked LMR phenomenon in the sensor configurations where the ZrO_2 layer is present. This aspect is very interesting because it would be possible to monitor both resonances (LMR and SPR) when to realize specific biosensors these kinds of configurations are used combined with self-assembled monolayer of bioreceptors.

SUPPORTING INFORMATION

- Outline of the construction process and structure of the SPR-POF reference sensor, with the refractive indices (n) and the dimensions.
- Thicknesses and refractive indexes of TiO2 and ZrO2 thin films prepared by DUV irradiation
- FTIR characterization of the TiO2 and ZrO2 before and after DUV irradiation
- Simulated SPR spectra for each design, for different external refractive index.

ACKNOWLEDGEMENT

The authors thank Simon Gree for FTIR characterization and the French Agence Nationale de la Recherche for fundings (project DYNABIO, grant ANR-19- CE19-0012 and NIRTRONIC, grant ANR-18-CE24-0028). This work was supported by the VALERE program of the University of Campania "Luigi Vanvitelli" (Italy), CAMPANIA project.

REFERENCES

[1] Singh, P. SPR Biosensors: Historical Perspectives and Current Challenges. *Sens. Actuat. B Chem*. **2016**, *229*, 110–130.

[2] Homola, J. Surface Plasmon Resonance Sensors for Detection of Chemical and Biological Species *Chem. Rev.* **2008**, *108* (2), 462–493.

[3] Nguyen, H.; Park, J.; Kang, S.; Kim, M. Surface Plasmon Resonance: A Versatile Technique for Biosensor Applications. *Sensors* **2015**, *15* (5), 10481−10510.

[4] Tong, L.; Wei, H.; Zhang, S.; Xu, H. Recent Advances in Plasmonic Sensors. *Sensors* **2014**, *14*, 7959-7973.

[5] Unser, S.; Bruzas, I.; He, J.; Sagle, L. "Localized Surface Plasmon Resonance Biosensing: Current Challenges and Approaches," *Sensors* **2015**, *15*, 15684-15716.

[6] Vitoria, I.; Ruiz Zamarreño, C.; Ozcariz, A.; Matias, I.R. Fiber Optic Gas Sensors Based on Lossy Mode Resonances and Sensing Materials Used Therefor: A Comprehensive Review. *Sensors* **2021**, 21, 731.

[7] Del Villar, I.; Arregui, F. J.; Zamarreño, C. R.; Corres, J. M.; Bariain, C.; Goicoechea, J.; Elosua, C.; Hernaez, M.; Rivero, P. J.; Socorro, A. B.; Urrutia, A.; Sanchez, P.; Zubiate, P.; Lopez,

D.; De Acha, N.; Ascorbe, J.; Matias, I. R. Optical sensors based on lossy-mode resonances, *Sens. Actuat. B Chem.* **2017**, *240*, 174-185.

[8] Zhao, Y.; Tong, R.; Xia, F.; Peng, Y. Current status of optical fiber biosensor based on surface plasmon resonance. *Biosens. Bioelectron.* **2019**, *142*, 111505.

[9] Esfahani Monfared, Y. Overview of Recent Advances in the Design of Plasmonic Fiber-Optic Biosensors. *Biosensors* **2020**, *10*, 77.

[10] Cennamo, N.; Pesavento, M.: Zeni, L. A review on simple and highly sensitive plastic optical fiber probes for bio-chemical sensing. *Sens. Actuat. B-Chem.* **2021**, *331*, 129393.

[11] Wang, X.; Wolfbeis, O.S. Fiber-Optic Chemical Sensors and Biosensors (2015–2019). *Anal. Chem.* **2020**, *92*, 397–430.

[12] Rani, M.; Sharma, N. K.; Sajal, V. “Localized surface plasmon resonance based fiber optic sensor with nanoparticles,” *Opt. Commun.* **2013**, *292*, 92-100.

[13] Lee, S.; Song, H.; Ahn, H.; Kim, S.; Choi, J.-r.; Kim, K. Fiber-Optic Localized Surface Plasmon Resonance Sensors Based on Nanomaterials. *Sensors* **2021**, *21*, 819.

[14] Luo, W.; Li, X.; Meng, J.; Wang, Y.; Hong, X. Surface Plasmon Resonance Sensor Based on Side-Polished D-Shaped Photonic Crystal Fiber With Split Cladding Air Holes. *IEEE T. Instrum. Meas.* **2021**, *70*, 1-11.

[15] Cennamo, N.; Massarotti, D.; Conte, L.; Zeni, L. Low Cost Sensors Based on SPR in a Plastic Optical Fiber for Biosensor Implementation. *Sensors* **2011**, 11, 11752-11760.

[16] De-Jun, F.; Mao-Sen, Z.; Liu, G.; Xi-Lu, L.; Dong-Fang, J. D-Shaped Plastic Optical Fiber Sensor for Testing Refractive Index. *IEEE Sens. J.* **2014**, *14*, 1673-1676.

[17] Cennamo, N.; D'Agostino, G.; Donà, A.; Dacarro, G.; Pallavicini, P.; Pesavento, M.; Zeni, L. Localized Surface Plasmon Resonance with Five-Branched Gold Nanostars in a Plastic Optical Fiber for Bio-Chemical Sensor Implementation. *Sensors* **2013**, *13*, 14676-14686.

[18] Verma, R.K.; Sharma, A.K.; Gupta, B.D. Surface plasmon resonance based tapered fiber optic sensor with different taper profiles. *Opt. Commun.* **2008**, *281*, 1486–1491.

[19] Kumar, S.; Sharma, G.; Singh, V. Sensitivity of tapered optical fiber surface plasmon resonance sensors. *Opt. Fiber Technol.* **2014**, *20,* 333–335.

[20] Kumar, S.; Kaushik, B. K.; Singh, R.; Chen, N.-K.; Yang, Q. S.; Zhang, X.; Wang, W.; Zhang, B. LSPR-based cholesterol biosensor using a tapered optical fiber structure. *Biomed. Opt. Express* **2019**, *10,* 2150-2160.

[21] Cennamo, N.; Arcadio, F.; Minardo, A.; Montemurro, D.; Zeni, L. Experimental Characterization of Plasmonic Sensors Based on Lab-Built Tapered Plastic Optical Fibers. *Appl. Sci.* **2020**, *10*, 4389.

[22] Liu, Q.; Jiang, Y.; Sun, Y.; Hu, C.; Sun, J.; Liu, C.; Lv, J.; Zhao, J.; Yi, Z.; Chu, P.K. Surface plasmon resonance sensor based on U-shaped photonic quasi-crystal fiber. *Appl. Opt.* **2021**, *60,* 1761-1766.

[23] Christopher, C., Subrahmanyam, A.; Sai, V.V.R. Gold Sputtered U-Bent Plastic Optical Fiber Probes as SPR- and LSPR-Based Compact Plasmonic Sensors. *Plasmonics* **2018**, *13*, 493–502.

[24] Cennamo, N.; Zeni, L.; Arcadio, F.; Catalano, E.; Minardo, A. A Novel Approach to Realizing Low-Cost Plasmonic Optical Fiber Sensors: Light-Diffusing Fibers Covered by Thin Metal Films. *Fibers* **2019**, *7,* 34.

[25] Liu, L.; Deng, S.; Zheng, J.; Yuan, L.; Deng, H.; Teng, C. An Enhanced Plastic Optical Fiber-Based Surface Plasmon Resonance Sensor with a Double-Sided Polished Structure. *Sensors* **2021**, *21*, 1516.

[26] Han, H.; Hou, D.; Luan, N.; Bai, Z.; Song, L.; Liu, J.; Hu, Y. Surface Plasmon Resonance Sensor Based on Dual-Side Polished Microstructured Optical Fiber with Dual-Core. *Sensors* **2020**, *20*, 3911.

[27] Xie, T., He, Y., Yang, Y.; Zhang, H.; Xu, Y. Highly Sensitive Surface Plasmon Resonance Sensor Based on Graphene-Coated U-shaped Fiber. *Plasmonics* **2021**, *16*, 205–213.

[28] Zhang, N.M.Y.; Li, K.; Qi, M.; Wu, Z. Hybrid Fiber-Optic Sensors. In: Wei L. (eds) Advanced Fiber Sensing Technologies. Progress in Optical Science and Photonics, Springer, Singapore **2020**, *9*, 13-38.

[29] Chen, C.-H.; Chiang, C.-Y.; Wu, C.-W.; Wang, C.-T.; Chau, L.-K. Integrated Graphene Oxide with Noble Metal Nanoparticles to Develop High-Sensitivity Fiber Optic Particle Plasmon Resonance (FOPPR) Biosensor for Biomolecules Determination. *Nanomaterials* **2021**, *11*, 635.

[30] Tabassum, R.; Gupta, B. D. Influence of Oxide Overlayer on the Performance of a Fiber Optic SPR Sensor With Al/Cu Layers. *IEEE J. Sel. Top. Quant.* **2017**, *23*, 81-88.

[31] Usha, S.P.; Mishra, S.K.; Gupta, B.D. Fabrication and Characterization of a SPR Based Fiber Optic Sensor for the Detection of Chlorine Gas Using Silver and Zinc Oxide. *Materials* **2015**, *8*, 2204-2216.

[32] Saad, Y.; Selmi, M.; Gazzah, M.H.; Bajahzar, A.; Belmabrouk, H. Performance enhancement of a copper-based optical fiber SPR sensor by the addition of an oxide layer. *Optik* **2019**, *190*, 1-9.

[33] Singh, H.; Raghuwanshi, S.K. Titanium dioxide (TiO2) coated optical fiber-based SPR sensor in near-infrared region with bimetallic structure for enhanced sensitivity. *Optik* **2021**, *226*, 165842.

[34] Biswas, P. K. Sol–gel thin films for optics and photonics. *J. Sol-Gel Sci. Technol.* **2011**, *59*, 456-474.

[35] Liang, L.; Xu, Y.; Wu, D.; Sun, Y. A simple sol–gel route to ZrO2 films with high optical performances. *Mater. Chem. Phys.* **2009**, *114*, 252-256.

[36] Park, Y.M.; Daniel, J.; Heeney, M.; Salleo, A. Room- Temperature Fabrication of Ultrathin Oxide Gate Dielectrics for Low- Voltage Operation of Organic Field- Effect Transistors. *Adv. Mater.* **2011**, *23*, 971-974.

[37] Yeh, C.C.; Zan, H.W.; Soppera, O. Solution-Based Micro- and Nanoscale Metal Oxide Structures Formed by Direct Patterning for Electro-Optical Applications. *Adv. Mater.* **2018**, 30, 1800923.

[38] Yeh, C.C.; Liu, H.C.; Heni, W.; Berling, D.; Zan, H.W.; Soppera, O. Chemical and structural investigation of zinc-oxo cluster photoresists for DUV lithography. *Journal of Materials Chemistry C* **2017**, 5 (10), 2611-2619.

[39] Yeh, C.C.; Liu, H.C.; Chuang, M.Y.; Denzer, J.; Berling, D.; Zan, H.W.; Soppera, O. Controllable Formation of Zinc Oxide Micro- and Nanostructures via DUV Direct Patterning. *Advanced Materials Interfaces* **2016**, 3 (19), 12.

[40] Lin, H.-C.; Stehlin, F.; Soppera, O.; Zan, H.-W.; Li, C.-H.; Wieder, F.; Ponche, A.; Berling, D.; Yeh, B.-H.; Wang, K.-H. Deep ultraviolet laser direct write for patterning sol-gel InGaZnO semiconducting micro/nanowires and improving field-effect mobility. *Sci. Rep.* **2015**, *5*, 10410.

[41] Stehlin, F.; Wieder, F.; Spangenberg, A.; Le Meins, J.-M.; Soppera, O. Room-temperature preparation of metal-oxide nanostructures by DUV lithography from metal-oxo clusters. *Journal of Materials Chemistry C* **2014**, *2*, 277-285.

[42] Mollah, Md. A.; Islam, Md. S. Novel Single Hole Exposed-Suspended Core Localized Surface Plasmon Resonance Sensor. *IEE Sens. J.* **2021**, *21*, 2813-2820.

[43] Islam, Md. S.; Islam, M. R.; Sultana, J.; Dinovitser, A.; Ng, B. W.-H.; Abbott, D. Exposed-core localized surface plasmon resonance biosensor. *J. Opt. Soc. Am. B* **2019**, *36*, 2306-2311.

[44] Fang, H.; Wei, C.; Wang, D.; Yuan, L.; Jiao, S.; Bao, Z.; Yang, H. Research on photonic crystal fiber based on a surface plasmon resonance sensor with segmented silver-titanium dioxide film. *J. Opt. Soc. Am. B* **2020**, *37*, 736-744.

[45] Edwards, D. A.; Hayward, R. N. Transition Metal Acetates. *Can. J. Chem.* **1968**, *46* (22), 3443–3446.

[46] Barboux-Doeuff, S.; Sanchez, C. Synthesis and Characterization of Titanium Oxide-Based Gels Synthesized from Acetate Modified Titanium Butoxide Precursors. *Mater. Res. Bull.* **1994**, *29* (1), 1–13.

[47] Kanso, M.; Cuenot, S.; Louarn, G. Sensitivity of Optical Fiber Sensor Based on Surface Plasmon Resonance: Modeling and Experiments. *Plasmonics* **2008**, *3*, 49-57.

Table of Contents (TOC) graphic